Guided wavefield curvature imaging of invisible damage in composite structures

Ganggang Sha[1], Hao Xu[2], Maciej Radzieński[3], Maosen Cao[1*], Wiesław Ostachowicz[3],

and Zhongqing Su[4]

[1]College of Mechanics and Materials, Hohai University, Nanjing 211100, China

[2]School of Aeronautics and Astronautics, Faculty of Vehicle Engineering and Mechanics, State Key Laboratory of Structural Analysis for Industrial Equipment, Dalian University of Technology, Dalian 116024, China

[3]Institute of Fluid-Flow Machinery, Polish Academy of Sciences, Gdansk 80-231,

[4]Department of Mechanical Engineering, The Hong Kong Polytechnic University, Kowloon, Hong Kong Special Administrative Region

[*]cmszhy@hhu.edu.cn

1

Abstract

Guided wavefields in composite structures carry a wealth of information about wavefield anomalies from damage–wave interactions. Although such anomalies can be used for damage detection, they are easily masked by incident waves from actuators and reflected waves from structural boundaries. This research presents a concept of guided wavefield curvature for the detection of structural damage. Wavefield curvature analysis is able to highlight the amplitudes of local anomalies in the wavefield signals associated with damage. A wavefield curvature imaging algorithm is developed for visualizing invisible damage in composite structures. The algorithm is first verified by detecting delamination in a carbon fiber reinforced polymer (CFRP) plate and then applied for detection of debonding in a honeycomb sandwich panel. In the experiments, wavefields are generated by a PZT transducer and are then registered by a scanning laser Doppler vibrometer. The experimental results accord well with the actual locations, sizes, and shapes of the delamination and debonding, confirming the effectiveness of the proposed algorithm for the detection of invisible damage in composite structures.

Keywords: damage imaging; guided wavefield curvature; CFRP plate; delamination; honeycomb sandwich panel; debonding

1. Introduction

Composite structures are widely adopted for critical components in civil, mechanical, and aerospace industries, owing to their high specific stiffness and strength, low weight, and corrosion resistance. These composite structures are often exposed to manufacturing defects and in-service damage, such as delamination. The presence of delamination causes severe degradation of the mechanical behavior of structures and even leads to structural failure. So, the study of the vibration characteristics of delaminated composite structures and the detection of delaminations are very important to ensure structural integrity and safety. Ju et al. [1] conducted finite element analysis of free vibration of composite plates with multiple delaminations. The results showed that the effect of delaminations on the natural frequencies and mode shapes of delaminated composite plates depended not only on the sizes, locations, and the number of delaminations but also on the boundary conditions. Mohanty et al. [2] investigated extensively the effect of various parameters including delamination size, boundary conditions, number of layers, fiber orientation, and aspect ratio on the natural frequencies of delaminated composite plates by both numerical and experimental cases. Panda et al. [3] carried out a combined numerical and experimental study on free vibration behavior of delaminated composite plates subjected to hygrothermal environment. The natural frequencies of delaminated composite plates were found to decrease with increase in uniform moisture content and temperature. The detection of delaminations based on vibration characteristics such as natural frequencies has been reported by many researchers [4,5]. Apart from vibration characteristics, guided waves show strong potential in damage detection due to their sensitivity to small damage and capability of travelling over a long distance [6–9,37,38]. A recent trend in guided-wave-based methods is the use of wavefield imaging, because advanced

equipment such as the scanning laser Doppler vibrometer (SLDV) enables the registration of dense wavefield data of the inspected structures [10–17]. The guided wavefields in terms of time and space dimensions carry a wealth of information about wavefield anomalies from damage–wave interactions. These anomalies can be employed for damage detection aided by wavefield analysis methods. Existing wavefield analysis methods are summarized here.

The simplest wavefield analysis method shows a series of wavefield images as a movie, from which damage can be viewed by observation of wavefield anomalies such as scattered waves at damage locations [10,11,18]. However, this method relies on the experience of the technician and is restricted to qualitative detection of damage in simple structures. A straightforward alternative is the creation of a damage map. Ruzzene et al. [19] proposed a root mean square (RMS)-based damage map creation method by calculating the RMS values of the wavefield data. Zak et al. [20] and Saravanan et al. [21] adopted the weighted RMS method to achieve better imaging results. Sohn et al. [22] used a similar concept of accumulated energy map of the wavefield data. It should be noted that wavefield anomalies induced by small damage are much weaker than the incident waves from actuators and the reflected waves from boundaries. Thus, it is desirable to remove incident waves from actuators and reflected waves from boundaries or to isolate wavefield anomalies associated with damage. Dawson et al. [23] proposed wavefield baseline subtraction method to isolate damage-induced wavefield anomalies by subtracting the baseline wavefield from the wavefield of a damaged structure. Often, however, the baseline wavefield from an intact structure is unavailable. Thus, researchers have developed several baseline-free analysis methods in the wavenumber domain with the aims of reducing noise, filtering a single mode of waves or waves in a range of propagation directions, and isolating wavefield

anomalies associated with damage. Ruzzene [24] developed a frequency-wavenumber domain filtering method to filter out incident waves by a three-dimensional Fourier transform (3D FT). Michaels et al. [25] used this method to remove incident waves and to separate multiple modes of waves. Sohn et al. [26,27] extracted standing waves for the imaging of delaminations and cracks aided by frequency-wavenumber domain filtering. Kudela et al. [28] presented a refined filtering method named adaptive wavenumber filtering method, in which a filter mask is constructed in the wavenumber domain. In the foregoing wavenumber filtering methods, inverse FT must be used to transform filtered data back to the space domain. Leckey et al. [29,30] proposed a local wavenumber analysis method with high spatial resolution by using the windowed FT. To do this, the wavefield data should be multiplied by a fixed-size 2D window function, e.g. Hanning window.

The above-mentioned works are mainly based on wavenumber domain analysis and each type of method is with certain limitations as introduced above. A major problem of wavenumber domain analysis based on FT is that while FT provides rich information in wavenumber domain, it lacks the ability of data representation with high spatial resolution. Although local wavenumber analysis provides space–wavenumber representation of wavefield data, a major drawback is that the optimal window size is fixed and difficult to be determined. This research introduces a spatial domain analysis method, where the concept of wavefield curvature is proposed to amplify damage-induced local anomalies in wavefield signals. The concept of wavefield curvature is analogous to mode shape curvature in the literature [31–33]. Mode shape curvature has been proved more sensitive to damage than mode shape itself and has been successfully used for damage detection in composite structures. Similarly, this research shows that wavefield curvature is more sensitive to damage than wavefield

5

itself. Based on wavefield curvature, an invisible damage visualization method is developed using a wavefield curvature imaging algorithm.

The rest of this paper is organized as follows. Section 2 describes wavefield measurement of a carbon fiber reinforced polymer (CFRP) plate. Section 3 presents the steps of the proposed wavefield curvature imaging algorithm for delamination detection in the CFRP plate. Section 4 shows the application of the algorithm for detecting debonding in a honeycomb sandwich panel. Section 5 presents a comparative study, where the adaptive wavenumber filtering method is used for delamination imaging. Conclusions are presented in Section 6.

2. Wavefield measurement

The wavefields of a CFRP plate with delamination were measured using a SLDV (Polytec PSV-400) in the form of out-of-plane velocities.

2.1 Experimental description

An 8-ply CFRP plate with dimensions of $500 \times 500 \times 3$ mm^3 was fabricated, and the lay-up of fiber orientation of the plate is [0 90 0 90]$_s$. The Young's moduli of the fiber and matrix are approximately 275 and 3.5 GPa, respectively, although prior knowledge of material properties is not required in the presented method. An artificial delamination was introduced by inserting a 15×15 mm^2 Teflon film between the 2nd and 3rd plies during the fabrication process. The in-plane position and size of the delamination are shown in Fig. 1. The CFRP plate was hung up by two strings. The setup for wavefield measurement is presented in Fig. 2. Guided waves were excited by a round PZT transducer (Ceramtec Sonox P502), 10 mm in diameter, bonded at the center of the back-surface of the plate. A five-cycle sine signal with frequency of 50 kHz was

modulated using a Hanning window and then used as the excitation signal. The signal was generated by an arbitrary waveform generator (TTi TGA1241) and then amplified by a signal amplifier (Piezo Systems EPA-104). The scanning head of the SLDV was positioned properly to adjust the laser beam to be normal to the surface of the inspected specimen. The wavefield signals, in terms of out-of-plane velocities, were acquired in a square grid including 375×375 points, covering the entire surface of the specimen with a grid spacing of 1.34 mm in both x and y directions. At each measuring point, a total of 1 ms time responses were registered at a 512 kHz sampling frequency, producing 512 time frames. The measured wavefield signals were saved in the form of 3D data set as $v(x, y, t)$ (one time dimension and two space dimensions). The discrete form was denoted as $v[i, j, r]$ with $i = 1, 2, ..., M$ and $j = 1, 2, ..., N$ being the numbers of measuring points in the x and y directions, respectively; $r = 1, 2, ..., T$ being the number of time frames.
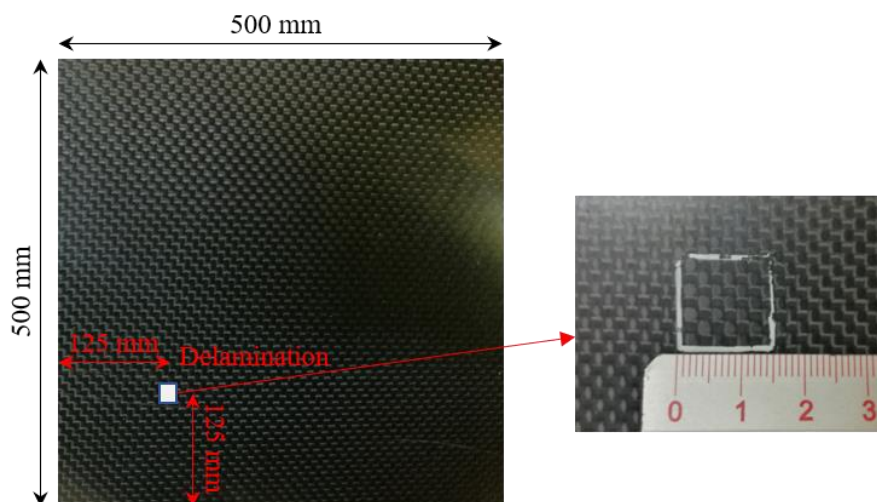

Fig. 1. Diagram of the inspected CFRP plate with a delamination.
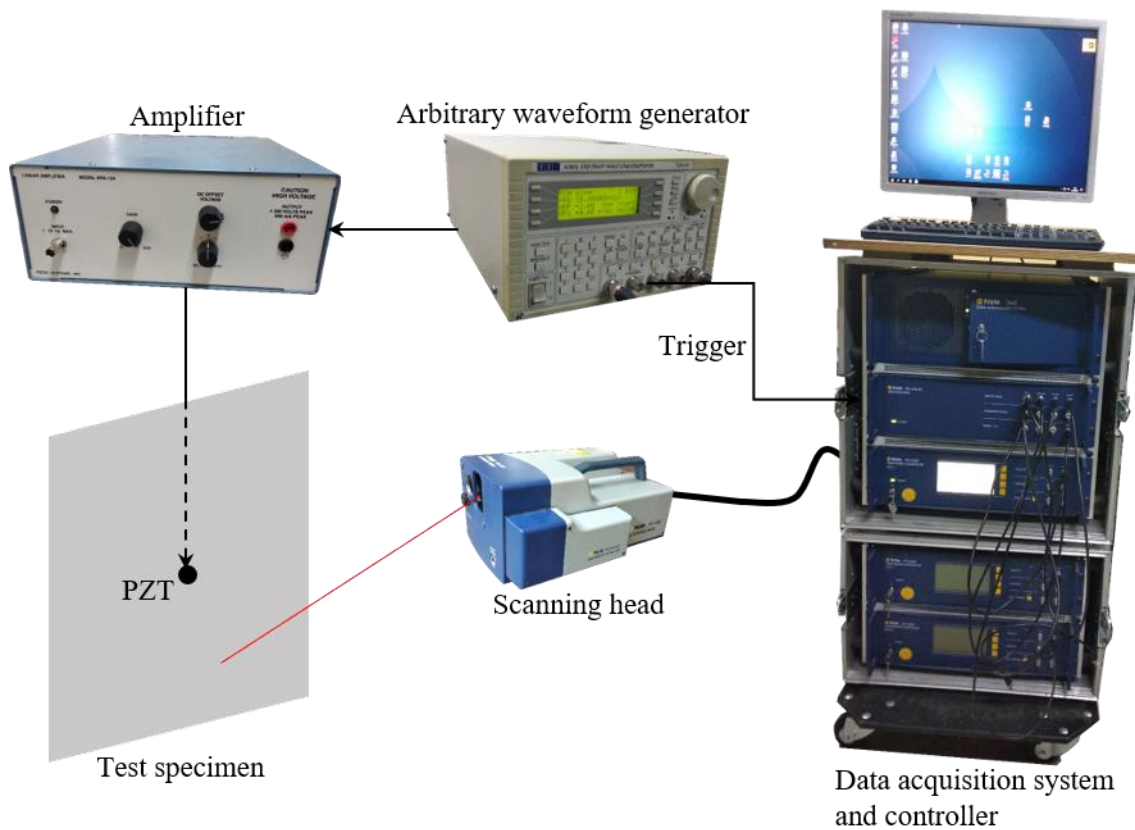
Fig. 2. Scheme of the wavefield measurement setup.

2.2. Wavefield images

Wavefield images of the CFRP plate at six arbitrarily chosen time frames are presented in Fig. 3. The following observations can be made from Fig. 3. At 57 µs, the incident waves emerge from the PZT transducer. Both A0 and S0 wave modes are excited and the A0 mode dominates the wavefield image. At 232 µs, the wavefront is beyond delamination and propagating waves are partially reflected and scattered from the delamination. At 406 µs, the waves are reflected from boundaries of the plate and weak scattered waves appear around delamination. Subsequently, scattering from the delamination is barely visible and the wavefield images are dominated by the main wave packages reflected from boundaries of the plate.
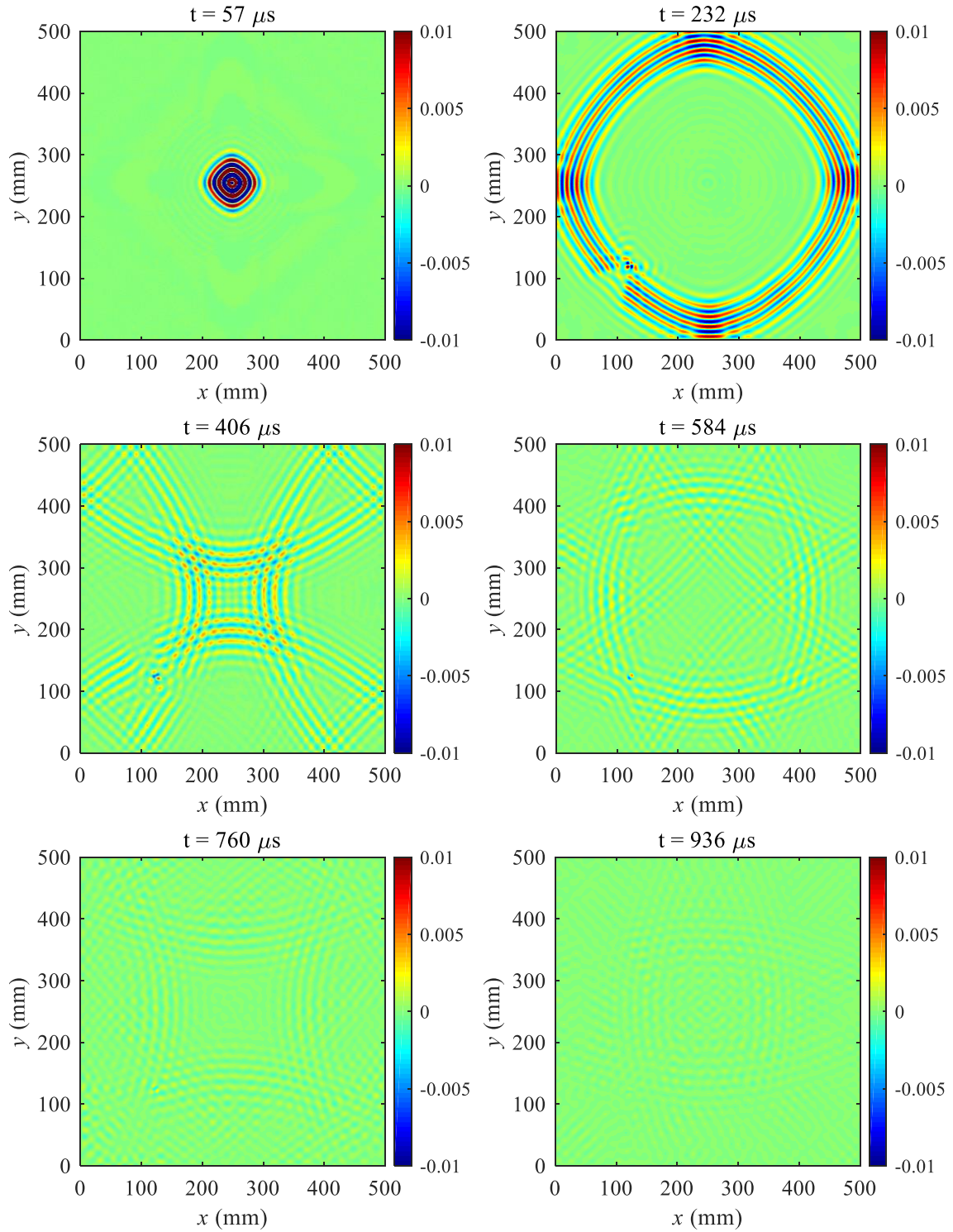
Fig. 3. Wavefield images at different time frames for the CFRP plate.

2.3 RMS map

The RMS map is achieved by calculating the RMS values of the wavefield data at all measuring points during the whole time history as

9

$$\mathrm{RMS}[i, j] = \sqrt{\frac{1}{T}\sum_{r=1}^{T}v^2[i, j, r]}, \tag{1}$$

where RMS[i, j] denotes the RMS value of the wavefield at measuring point [i, j].

Wave propagation can be seen as energy propagation from the actuator. Delamination in the inspected plate changes the distribution of the energy. Those changes in energy distribution are represented as anomalous regions in the RMS map and can be used for damage detection. Figure 4 (a) presents the RMS map for the inspected CFRP plate. A zoomed-in figure with adapted color scale focusing on the delamination region is presented in Fig. 4 (b). The anomalies in the central part in Fig. 4 (b) indicate the actual location of delamination. However, the shape and size of the delamination cannot be viewed clearly because of the interference of incident waves from the actuator and reflected waves from structural boundaries. Moreover, we are able to present the delamination region since it is known in advance. In practical cases without damage information, damage is more difficult to be identified from the RMS map due to the influence of the incident and reflected waves.
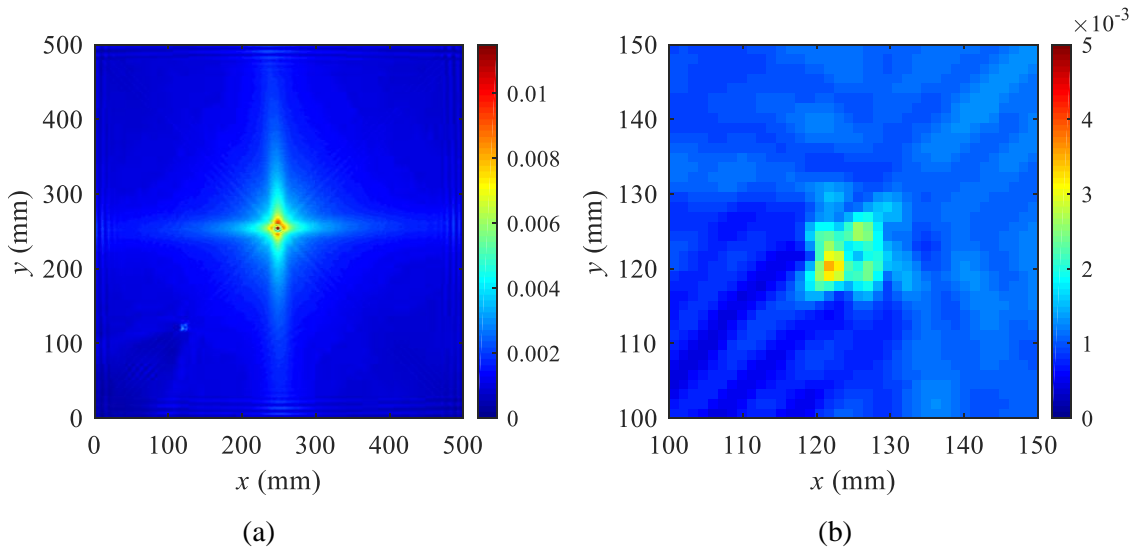

Fig. 4. (a) RMS map; (b) zoomed-in figure of the delamination region for the CFRP plate.

10

3. Wavefield curvature imaging algorithm

To reveal the shape and size of the delamination, a wavefield curvature imaging algorithm is developed to process the wavefield data. The proposed wavefield curvature imaging algorithm is schematically presented in Fig. 5, and the details of each step are described in the following sections.
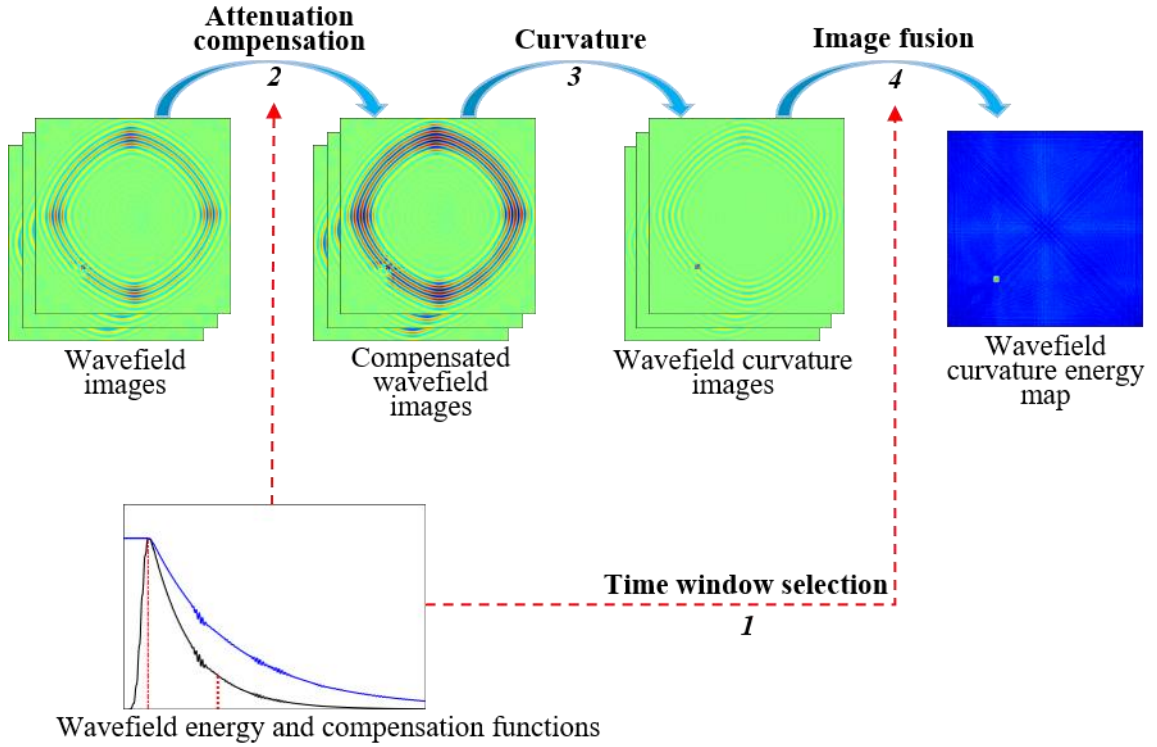

Fig. 5. Wavefield curvature imaging algorithm.

3.1 Selection of time window

Wavefield energy at each time frame *r* is determined as

$$E[r] = \sum_{i=1}^{M} \sum_{j=1}^{N} v^2[i, j, r],$$

(2)

where $E[r]$ is called wavefield energy function and represents wavefield energy dissipating with time. The normalized energy function is obtained as

$$E_N[r] = \frac{E[r]}{E_{max}},$$

(3)

11

where E_N denotes the normalized energy function. In accordance with Eqs. (2) and (3), the normalized energy function of the wavefields from the inspected CFRP plate is plotted with a black line in Fig. 6. It is evident from Fig. 6 that the wavefield energy increases from zero to the maximum and then attenuates to almost zero with time. Ripples in the energy function are caused by the reflection of the waves from edges.

Image fusion during a time window is conducted to create a final damage map in the following section. The time window used in image fusion is selected based on the presented energy function in Fig. 6. At the starting period, guided waves just propagate in a small area around the actuator (e.g. wavefield image at 57 µs in Fig. 3). Wavefield images during this period carry less information about damage and should be skipped in image fusion. At the ending period, the wavefield energy tends to zero indicating that the main components of guided waves dissipate and much noise exists (e.g. wavefield image at 936 µs in Fig. 3). Thus, wavefield images during the ending period do not need to be considered in image fusion. Accordingly, the starting point r_a of the time window was selected corresponding to the energy maximum in Fig. 6 to make sure that all guided waves were generated and well propagated. The time point at energy maximum roughly coincides with the end of the pulse of the excitation signal. The ending point r_b was selected at time frame when the normalized energy drops to a given threshold (5% here).
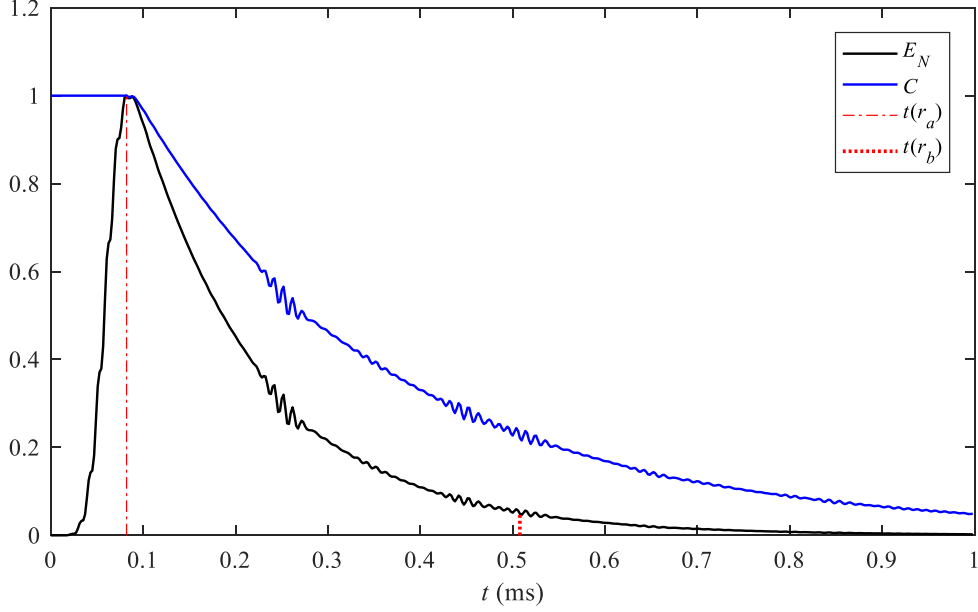
Fig. 6. Normalized energy function and corresponding compensation function.

3.2 Attenuation compensation

Decrease of wavefield energy in Fig. 6 is mostly due to energy dissipation from the material damping and/or energy radiation to the surroundings. This phenomenon creates difficulty in the detection of damage located further from the actuator. To minimize this effect, a compensation function denoted as $C[r]$ is introduced:

$$C[r] = \begin{cases} 1, & \text{if } r < r_a \\ \sqrt{E_N}, & \text{if } r \geq r_a \end{cases}.$$ (4)

The compensation function for the inspected CFRP plate is obtained from Eq. (4) and is plotted with a blue line in Fig. 6. The compensated wavefield is then obtained as

$$\bar{v}[i, j, r] = \frac{v[i, j, r]}{C[r]},$$ (5)

where $\bar{v}$ denotes the compensated wavefield. The original and compensated waveforms at the central measuring point are presented in Fig. 7. As seen from Fig. 7, the amplitudes of the compensated waveform are greater in the compensated parts.
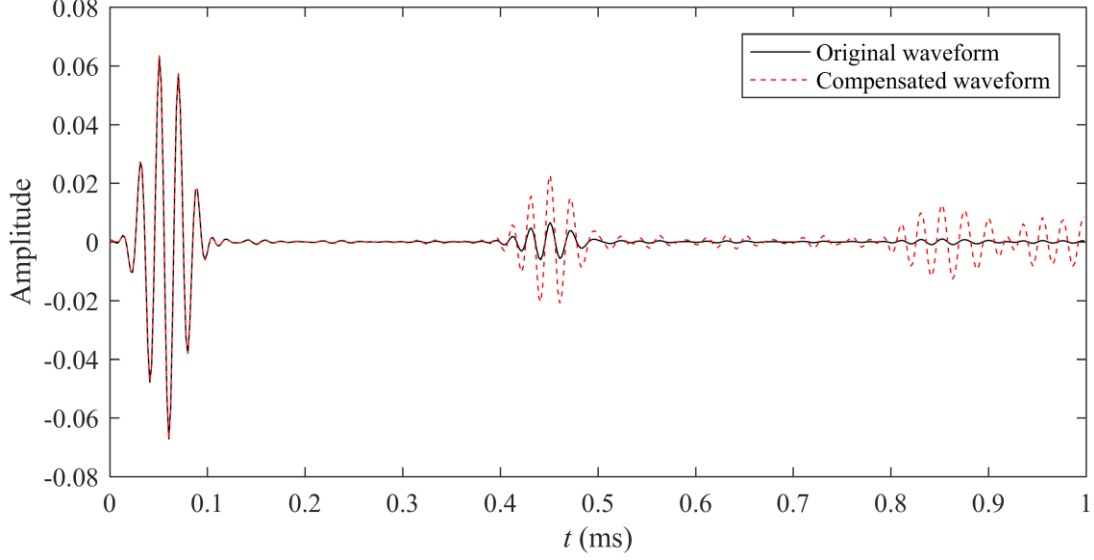
13

Fig. 7. Original and compensated waveforms at the central measuring point of the CFRP plate.
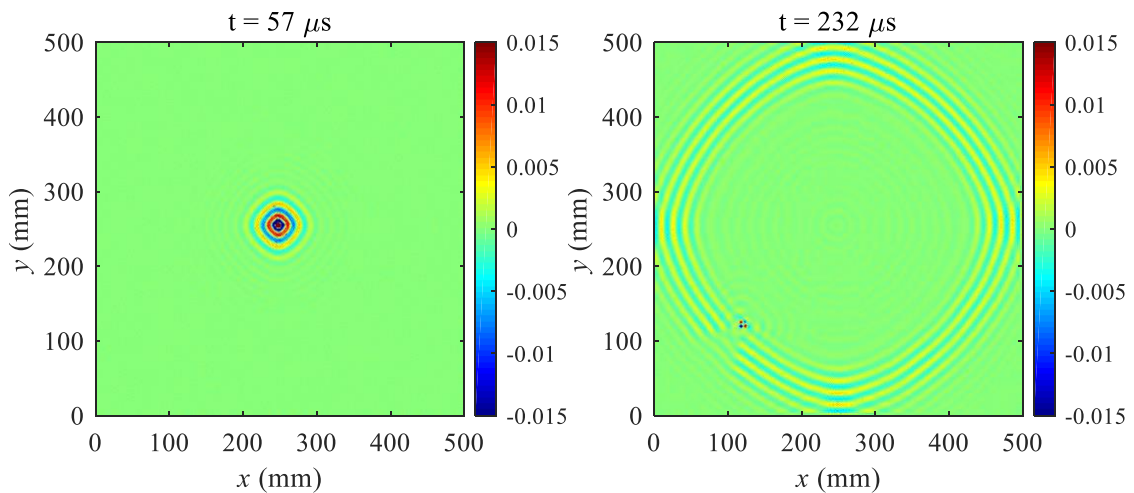
3.3 Wavefield curvature

Wavefield curvature is defined as the curvature of a wavefield image at each time frame. In the case of a plate, its wavefield curvature can be approximated by the central difference of the wavefield signal $\bar{v}[i,j,r]$ as

$$w[i,j,r] = \frac{\bar{v}[i+1,j,r] - 2\bar{v}[i,j,r] + \bar{v}[i-1,j,r]}{h_x^2} + \frac{\bar{v}[i,j+1,r] - 2\bar{v}[i,j,r] + \bar{v}[i,j-1,r]}{h_y^2},$$

(6)

where w denotes wavefield curvature, h_x and h_y are the grid spacings in the x and y directions, respectively. Curvatures are used mainly because of their higher-order derivative nature that is sensitive to local anomalies in wavefield signals associated with damage. For curvature construction, several factors need to be taken into account. For instance, for the current measurement technique, waves in A0 mode are more effective than in S0 mode in damage identification considering that the magnitudes of out-of-plane velocities in S0 mode are too small to be captured accurately. Another

14

factor is that in theory, the density of measuring points should be set larger enough to guarantee the accuracy of central difference. For other aspects, some principles for common wavefield-based methods should also be adopted by curvature-based method, e.g., wavelengths smaller than, or comparable to, damage size are often used to prevent failures of damage recognition.

The corresponding wavefield curvature images at the six time frames in Fig. 3 are shown in Fig. 8. In the calculation of wavefield curvature, the values of h_x and h_y are set to 1 for simplicity and such a setting has no effect on the quality of final damage imaging since the grid spacings in the x and y directions are equal. Compared with the wavefield images in Fig. 3, the main components of guided waves in the corresponding wavefield curvature images are mostly restrained and the delamination-induced anomalies are highlighted in these images. For better presentation, the corresponding wavefield curvature modulus images are depicted in Fig. 9, in which delamination-induced anomalies can be seen more clearly.
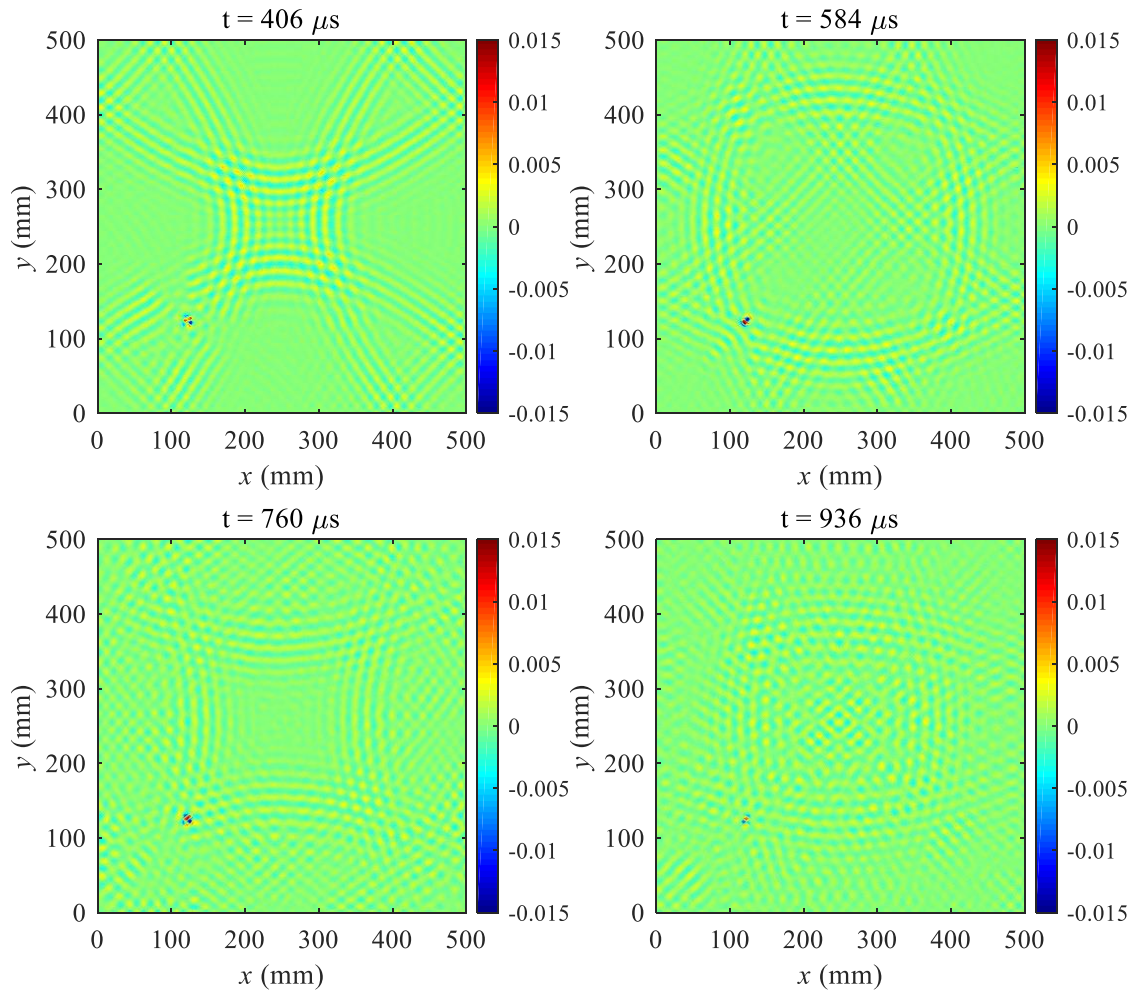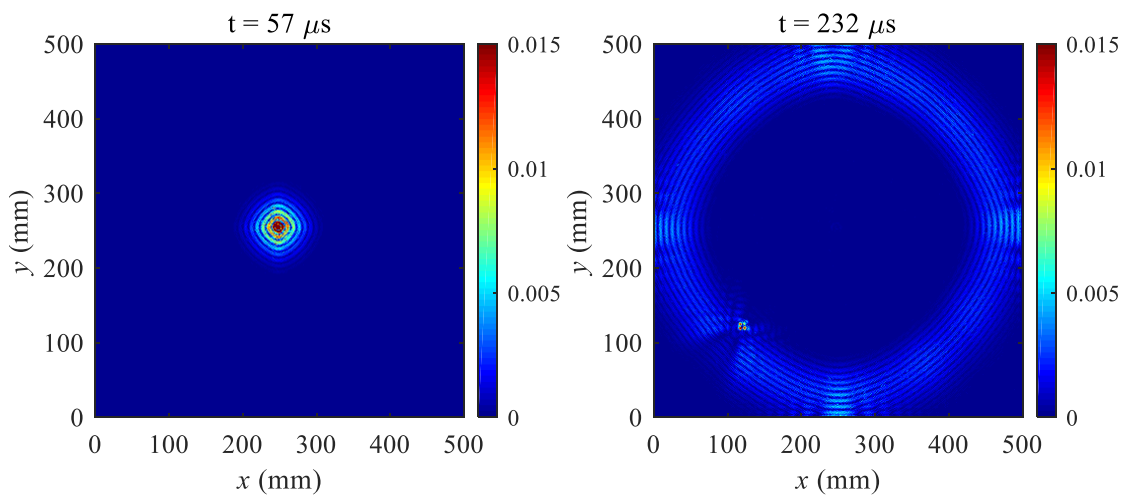
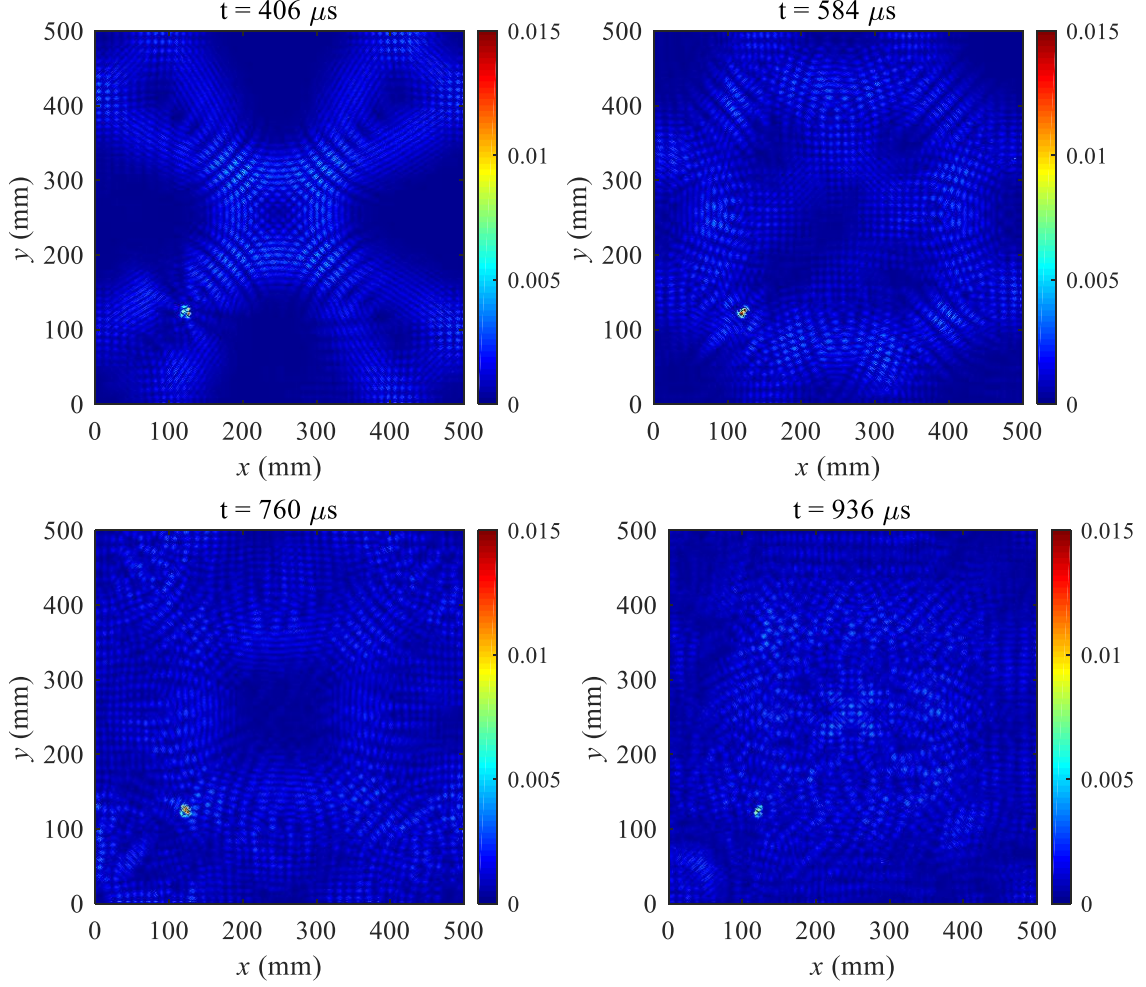**Fig. 8.** Wavefield curvature images at different time frames.

Fig. 9. Wavefield curvature modulus images at different time frames.

3.4 Image fusion

The wavefield curvature images during the selected time window are fused to create a final energy map:

$$E[i, j] = \sum_{r=r_a}^{r_b} w^2[i, j, r], \tag{7}$$

where $[r_a, r_b]$ is the time window selected in Section 3.1. The energy map $E[i, j]$ represents the energy distribution in space and is different from the energy function $E[r]$ that represents the energy dissipation with time.

The final wavefield curvature energy map of the inspected CFRP plate is shown in

Fig. 10 (a). Delamination in the CFRP plate is clearly visualized with its proper location, as shown in Fig. 10 (a). Its size and shape are obvious in the zoomed-in figure in Fig. 10 (b). Compared with the RMS map in Fig. 4 (a), the wavefield curvature energy map in Fig. 10 (a) performs better in revealing the actual location of the delamination. Moreover, it can be seen by comparing Fig. 10 (b) and Fig.4 (b) that wavefield curvature energy map is much superior in damage quantification, where the size and shape of the delamination are identified much more precisely in Fig. 10 (b) than in Fig. 4 (b).
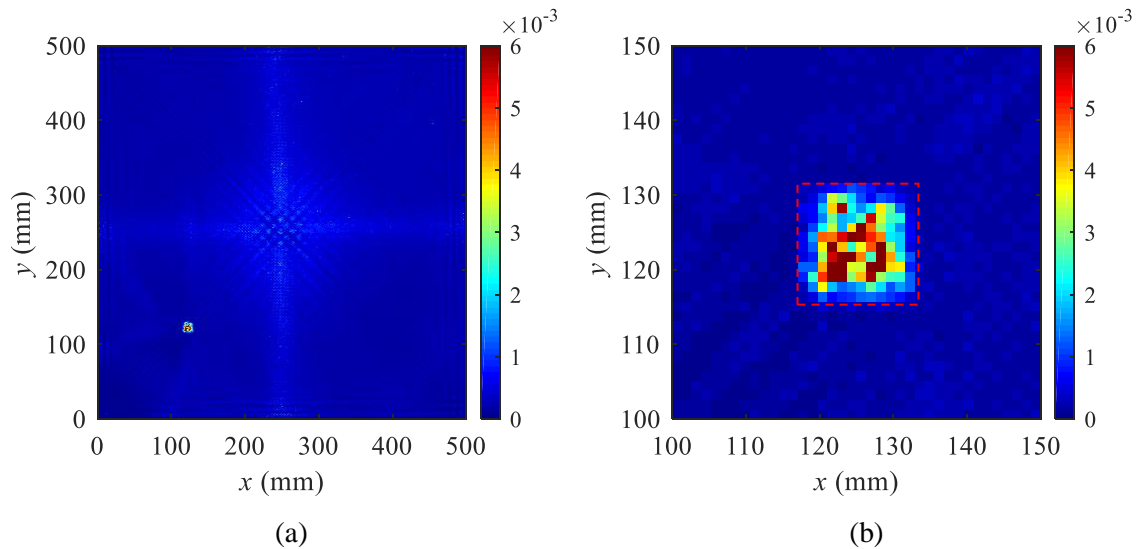

(a)   (b)

Fig. 10. (a) Wavefield curvature energy map; (b) zoomed-in figure of the delamination region (The dashed box indicates the region of delamination).

4. Application for detecting debonding in a honeycomb sandwich panel

Honeycomb sandwich panels have become popular currently due to their low weight and high stiffness. These structures are often subject to imperfect bonding during the fabrication process or debonding caused by impact. Due to the complex nature of such structures, the mechanism of guided wave propagation and its use for detection of debonding impose many challenges, in which researchers have made progress [34–36].

The proposed wavefield curvature imaging algorithm is utilized to detect debonding in a honeycomb sandwich panel with in-plane dimensions of 500 mm by 500 mm and thickness of 7 mm. The panel is made of two 1 mm thick 5005 aluminum surface plates (Fig. 11 (a)) with a 5 mm thick aluminum honeycomb core (Fig. 11 (b)) bonded between the plates by epoxy glue. The honeycomb core is composed of hexagonal cells. Each cell is made of 50 microns thick 3003 aluminum foil. During the fabrication process, the central area of the honeycomb core was not bonded to the front surface plate because about 125×125 mm^2 of the core in the central area was crushed. Additionally, two debonding regions were created by separating the inner core from the front and back plates, respectively. The front debonding is relatively small in an irregular shape which is about 160 mm long and 32 mm wide at the widest region. The back debonding is large in size as a quarter of a circle with a radius of 270 mm. The debonding regions in the specimen are presented in detail in Fig. 12. The sandwich panel was hung up by two light strings. The same type of PZT transducer used in Section 2 was attached on the back surface in the lower right corner as shown in Fig. 12. The excitation signal is a five-cycle sine signal with frequency of 5 kHz modulated with a Hanning window. Relatively low frequency was used due to the fact that excitation signals with high frequencies excite waves with shorter wavelengths which are not propagating well in such a structure and are more prone to interact with individual honeycomb cells, creating very complex patterns. The guided wavefields were measured by the SLDV in a square grid including 251×251 measuring points covering the entire front surface with a grid spacing of 2 mm in both x and y directions. The spacing is larger than that in the CFRP plate mainly because the wavelength in the honeycomb sandwich panel is longer and the damage sizes are larger. Thus, larger spacing distance is able to carry sufficient information about wave-damage interactions.

At each measuring point, responses in terms of out-of-plane velocities during a total of 20 ms were measured with sampling frequency of 51.2 kHz. The excitation position is not critical to the effectiveness of the method as long as the waves propagate through the entire inspected area.
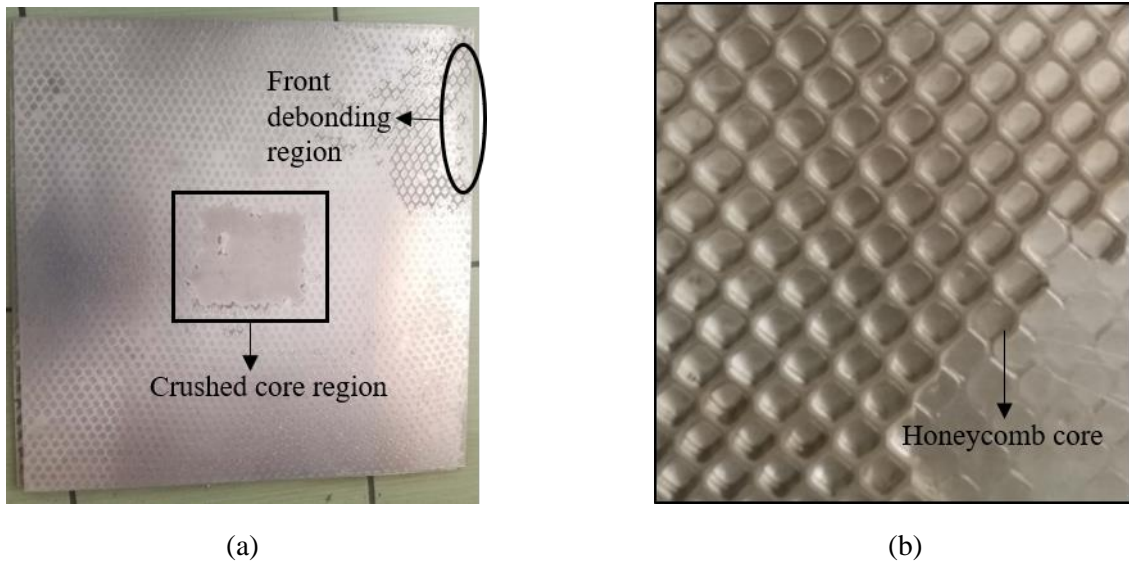

(a)   (b)

Fig. 11. (a) Front aluminum plate; (b) honeycomb core.
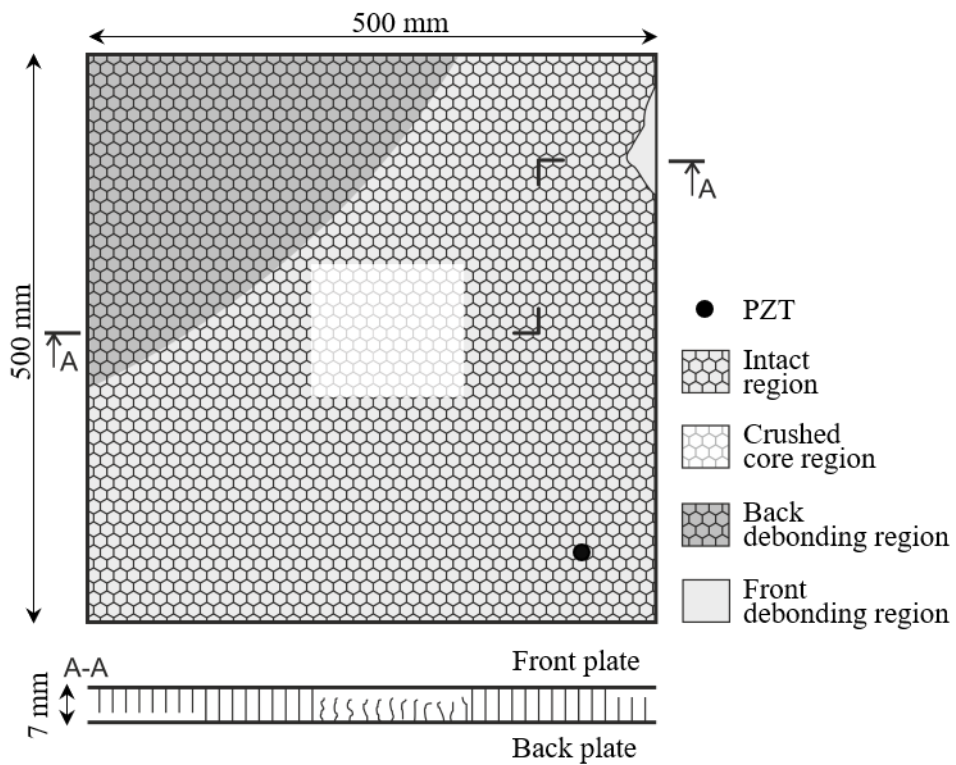

Fig. 12. Damage configuration in the honeycomb sandwich panel.

Wavefield images at arbitrary time frames are plotted in Fig. 13. Wave interaction with debonding regions can be seen from wavefield images at 2.7 ms and 5.06 ms. Wavefield image at 16.58 ms is also plotted in the form of 3D image in Fig. 14 (a). It should be noted that at some measuring points, outlier values were registered by SLDV as circled by black dashed boxes in Fig. 14 (a). These outliers can be smoothed by application of median filter with a grid of 2×2 points. The median filtered image is shown in Fig. 14 (b) in which the outliers are completely removed.
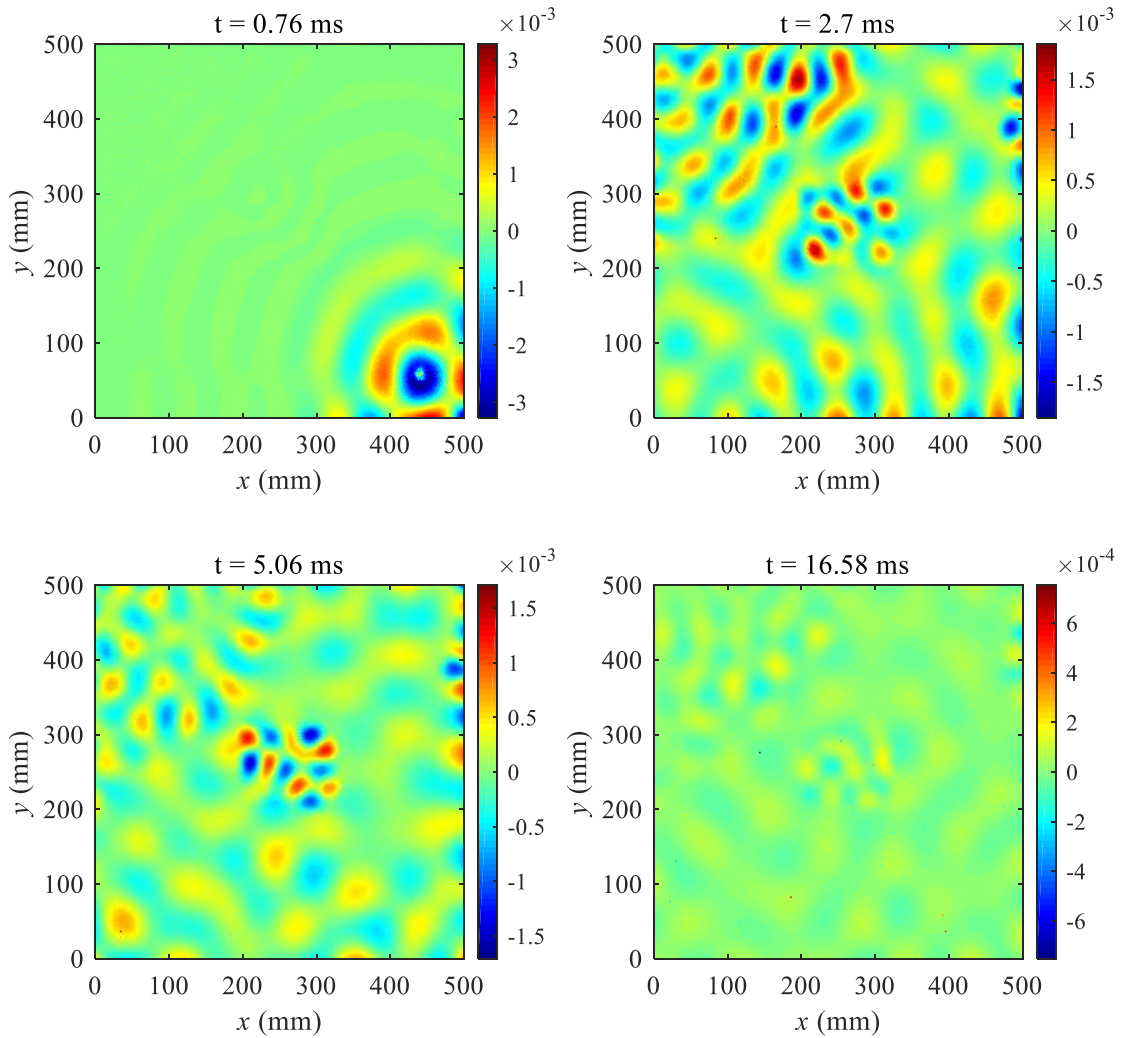

Fig. 13. Wavefield images at different time frames for the honeycomb sandwich panel.

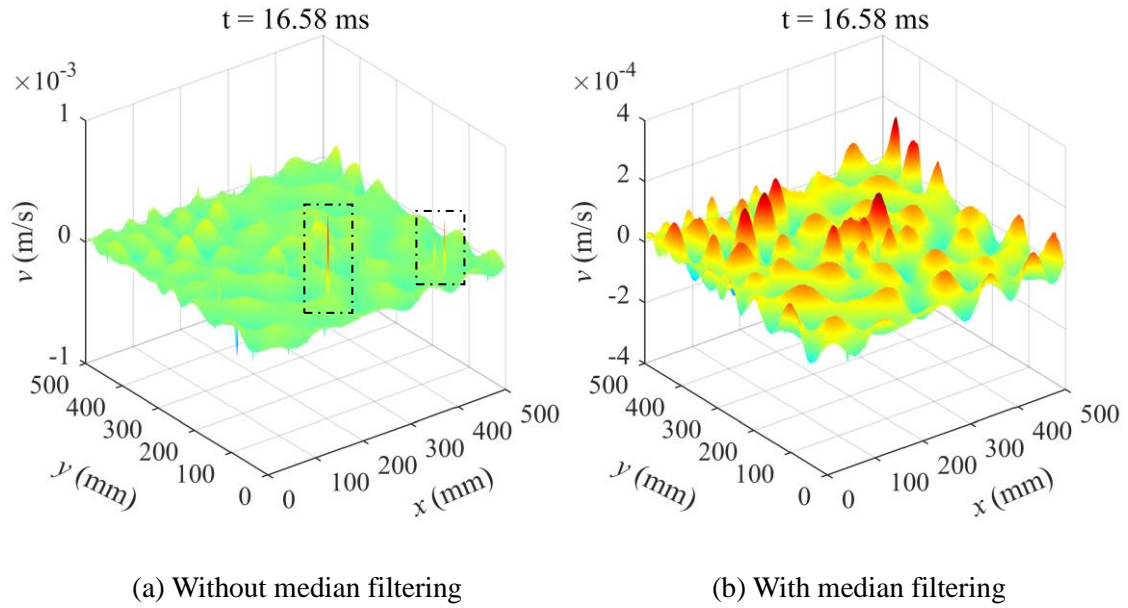(a) Without median filtering (b) With median filtering

Fig. 14. 3D wavefield images at 16.58 ms.

It is seen from Fig. 13 that wave propagation in the honeycomb sandwich panel looks more complex than that in the CFRP plate. Anomalous waves can be observed in the debonding regions, particularly in the crushed core region. However, it is difficult to assess the sizes or shapes of the debonding regions just from the wavefield images. The proposed wavefield curvature imaging algorithm is then utilized to process the wavefield data before and after median filtering. The ultimate wavefield curvature energy maps are obtained as described in Section 3 and are shown in Fig. 15. It is seen from Fig. 15 (a) that without median filtering, the debonding regions can still be observed, but with lower identification accuracy because of the existence and interference of singular color points in the damage map deemed as outliers. The outliers can be largely eliminated by using median filtering, as seen in Fig. 15 (b). It can be seen from Fig. 15 (b) that the curvature indication of the crushed core region and front debonding region is more significant than that of the back debonding region, in terms of

larger magnitudes and densities in the damaged regions. This is because the regions of crushed core and front debonding are closer to the scanned surface and thus are able to be identified more effectively. Interestingly, relatively discrete distribution of points of curvature indication is seen in the damaged regions, which is because the wave propagation is influenced by the periodic geometric features of the honeycomb cells.

To further investigate the performance of the present method in noisy environments, white Gaussian noise is added to the median filtered time-waveform signals. Noise level is defined by signal-to-noise ratio (SNR), and the situations under two SNR values, i.e., 40 and 10 dB, are investigated. The corresponding damage maps subject to the two noise levels are shown in Fig. 16. Under SNR of 40 dB, the damage map (in Fig. 16 (a)) shows large similarity with that in Fig. 15 (b) without noise, although the magnitudes of the curvature indication are slightly less prominent. Under SNR of 10 dB, however, noise interference becomes more intense, and the false alarm of damage at the excitation position is significant.
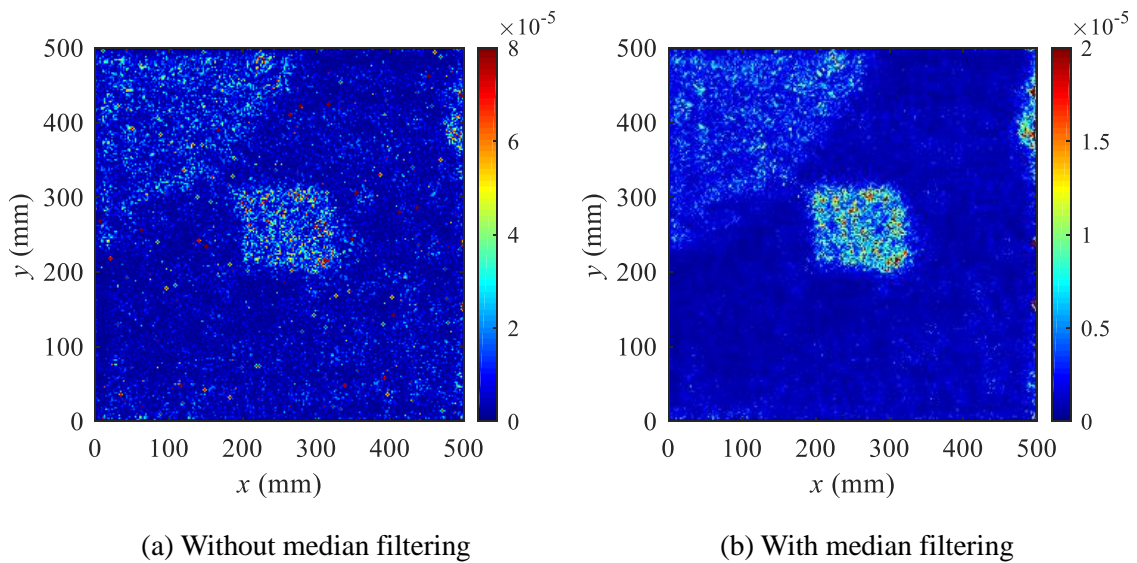

(a) Without median filtering   (b) With median filtering

Fig. 15. Wavefield curvature energy maps of the honeycomb sandwich panel.
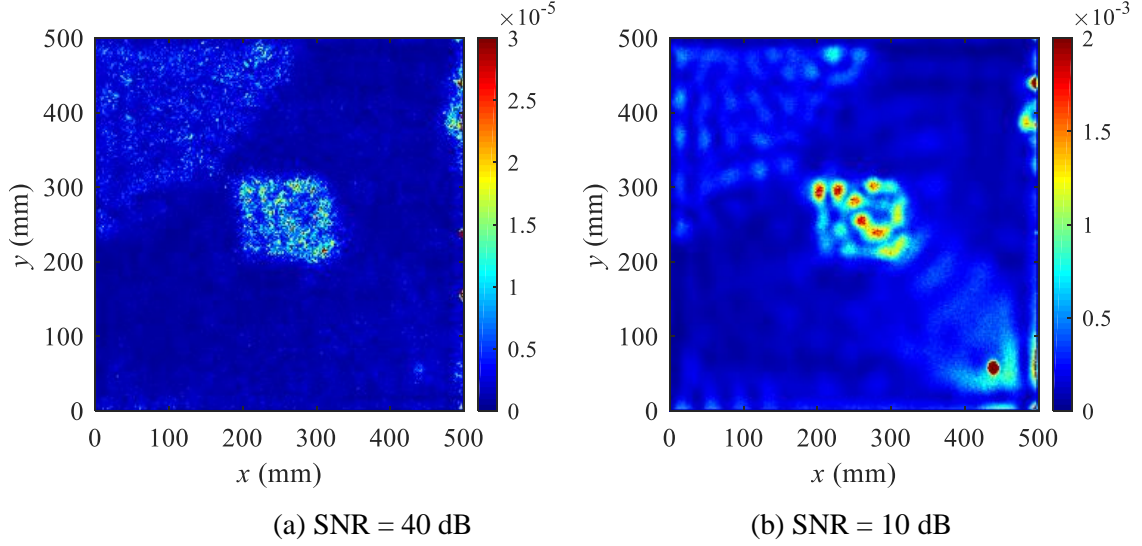
(a) SNR = 40 dB (b) SNR = 10 dB

Fig. 16. Wavefield curvature energy maps at different noise levels.

5. Comparative study

For comparison, a previously established wavefield imaging method, namely adaptive wavenumber filtering method [28], is used for delamination imaging in the CFRP plate. The procedures of the adaptive wavenumber filtering method are presented in Fig. 17, where the key step is to create a wavenumber filter. 2D FT of wavefield signal $v(x, y)$ is denoted as $V(k_x, k_y)$ with k_x and k_y being the wavenumbers in x and y directions, respectively. The wavenumber filter is obtained as

$$M(k_x, k_y) = \begin{cases} 0 & \text{if } V(k_x, k_y) > \text{threshold} \\ 1 & \text{otherwise} \end{cases}, \tag{8}$$

where $M(k_x, k_y)$ is the wavenumber filter mask. The optimal value of the threshold is determined by finding the value corresponding to 5% of the big values in the cumulative distribution function of all values in matrix V. Upon on the implementation of the adaptive wavenumber filtering method, the ultimate wavefield anomaly energy map for delamination imaging is shown in Fig. 18.
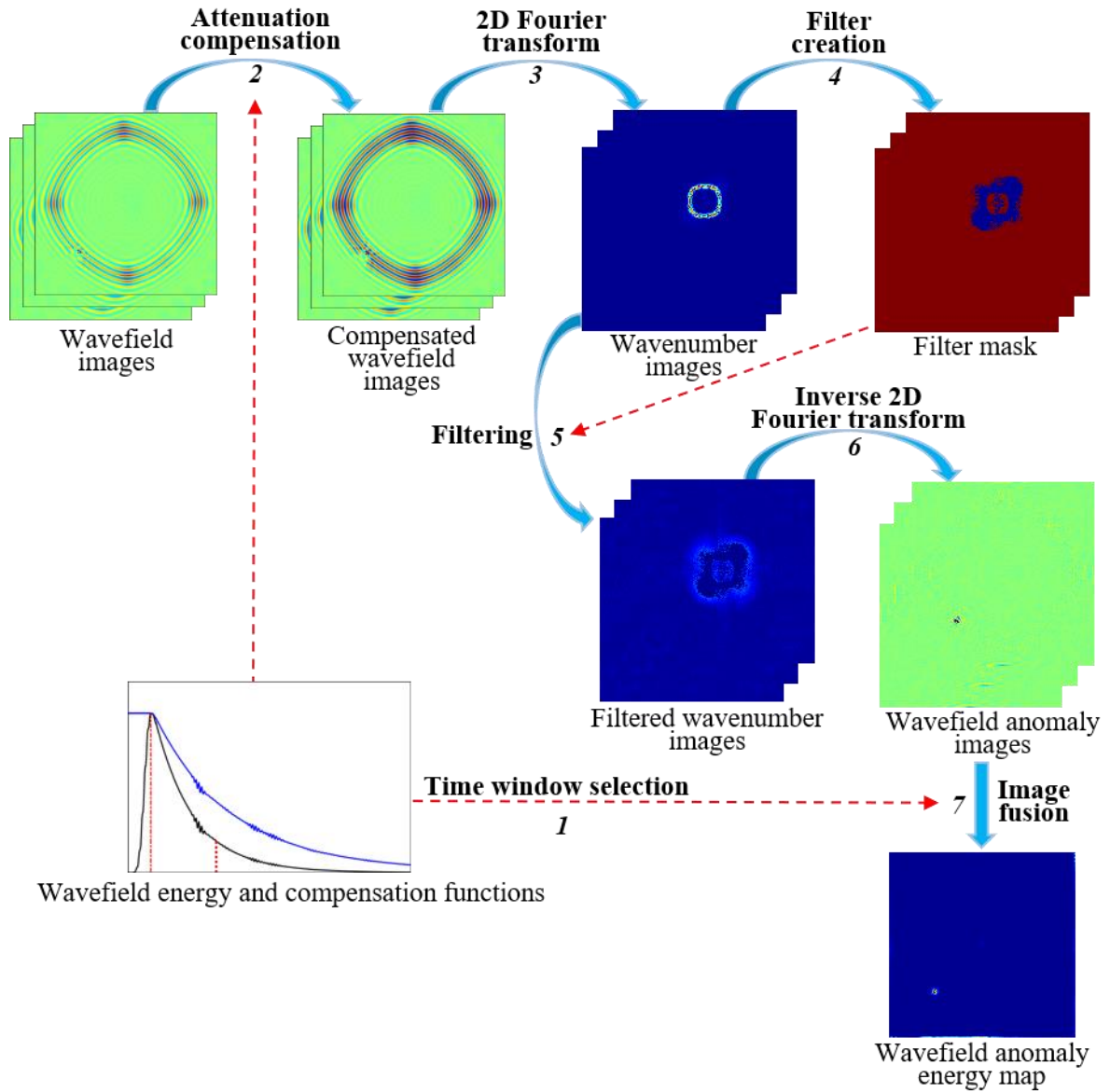
Fig. 17. Adaptive wavenumber filtering imaging algorithm.
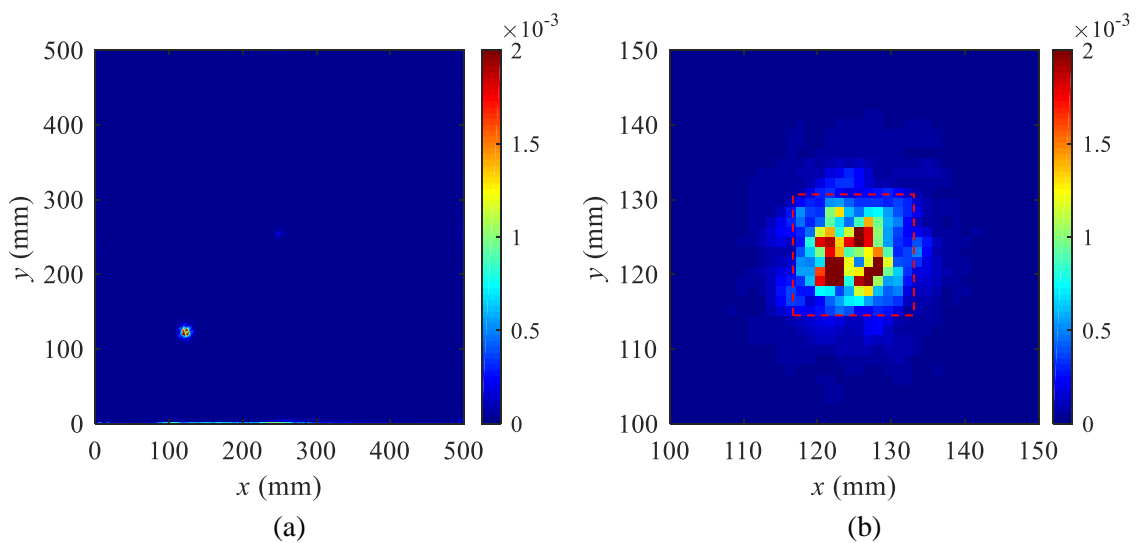

(a)

(b)

Fig. 18. (a) Wavefield anomaly energy map; (b) zoomed-in figure of the delamination region.

It can be seen that the adaptive wavenumber filtering method is also able to indicate the delamination position with good accuracy. However, superior capacity of the present method in characterizing the exact size and even shape of the delamination zone can be clearly seen by comparing Figs. 10 (b) and 18 (b). In addition, the present method also shows advantages in other aspects. For example, the algorithm of the present method shows much larger simplicity, as can be seen by comparing the procedures in Figs. 5 and 17. More importantly, the implementation of the present method shows relatively larger convenience, by recognizing that the optimal threshold of filter for the adaptive wavenumber filtering method need to be selected with sophistication.

6. Conclusions

In this paper, we propose a new concept of guided wavefield curvature. The guided wavefield curvature is proved to be more sensitive to damage than the wavefield itself. Based on the proposed guided wavefield curvature, an invisible damage imaging algorithm is developed to create a wavefield curvature energy map. The wavefield curvature energy map is successfully used for detection of both delamination in a CFRP plate and debonding in a honeycomb sandwich panel. The main advantages of the proposed algorithm are summarized as follows: (i) It provides a final damage map with high efficacy that is easily interpreted for damage detection; (ii) It is baseline-free without a priori information about reference state of the inspected structure; (iii) It is robust and versatile for detection of a wide variety of manufacturing defects and damage occurring in composite structures.

References

[1]   F. Ju, H.P. Lee, K.H. Lee, Finite element analysis of free vibration of delaminated composite plates, Compos. Eng. 5 (1995) 195–209. doi:10.1016/0961-9526(95)90713-L.

[2]   J. Mohanty, S.K. Sahu, P.K. Parhi, Numerical and experimental study on free vibration of delaminated woven fiber glass/epoxy composite plates, Int. J. Struct. Stab. Dyn. 12 (2012) 377–394. doi:10.1142/S0219455412500083.

[3]   H.S. Panda, S.K. Sahu, P.K. Parhi, Hygrothermal effects on free vibration of delaminated woven fiber composite plates – Numerical and experimental results, Compos. Struct. 96 (2013) 502–513. doi:10.1016/j.compstruct.2012.08.057.

[4]   J. Pan, H. Kumar Singh, W. Luo, K. Ram Ramakrishnan, Z. Zhang, Vibration-based delamination detection in curved composite plates, Compos. Part A Appl. Sci. Manuf. 119 (2019) 261–274. doi:10.1016/j.compositesa.2019.02.002.

[5]   G. Sha, M. Cao, M. Radzieński, W. Ostachowicz, Delamination-induced relative natural frequency change curve and its use for delamination localization in

laminated composite beams, Compos. Struct. 230 (2019) 111501.

doi:10.1016/j.compstruct.2019.111501.

[6]   S. Sikdar, S. Banerjee, Guided wave based nondestructive analysis of localized

inhomogeneity effects in an advanced sandwich composite structure, Compos.

Part B Eng. 176 (2019). doi:10.1016/j.compositesb.2019.107195.

[7]   Z. Su, L. Ye, Y. Lu, Guided Lamb waves for identification of damage in

composite structures: A review, J. Sound Vib. 295 (2006) 753–780.

doi:10.1016/j.jsv.2006.01.020.

[8]   W. Ostachowicz, M. Radzieński, P. Kudela, Comparison studies of full wavefield

signal processing for crack detection, Strain. 50 (2014) 275–291.

doi:10.1111/str.12098.

[9]   M. Mitra, S. Gopalakrishnan, Guided wave based structural health monitoring: A

review, Smart Mater. Struct. 27 (2016) 053001.

doi:10.1088/0964-1726/25/5/053001.

[10]   W.H. Leong, W.J. Staszewski, B.C.Lee, F. Scarpa, Structural health monitoring

using scanning laser vibrometry: III. Lamb waves for fatigue crack detection,

Smart Mater. Struct. 14 (2005). doi:10.1088/0964-1726/14/6/031.

[11]   T.E. Michaels, J.E. Michaels, B. Mi, M. Ruzzene, Damage detection in plate

structures using sparse ultrasonic transducer arrays and acoustic wavefield

imaging, in: AIP Conf. Proc., 2005: pp. 938–945. doi:10.1063/1.1916774.

[12]   B. Park, Y.K. An, H. Sohn, Visualization of hidden delamination and debonding

in composites through noncontact laser ultrasonic scanning, Compos. Sci.

Technol. 100 (2014) 10–18. doi:10.1016/j.compscitech.2014.05.029.

[13]   J. Druce, S. Gonella, M. Kadkhodaie, S. Jain, J.D. Haupt, Locating material

defects via wavefield demixing with morphologically germane dictionaries,

Struct. Heal. Monit. 16 (2017) 112–125. doi:10.1177/1475921716664515.

[14]   J.B. Harley, C.C. Chia, Statistical partial wavefield imaging using Lamb wave

signals, Struct. Heal. Monit. 17 (2018) 919–935.

doi:10.1177/1475921717727160.

[15]   Y.K. Esfandabadi, M. Bilodeau, P. Masson, L. Marchi, Deep learning for

enhancing wavefield image quality in fast non-contact inspections, Struct. Heal.

Monit. (2019) 1–12. doi:10.1177/1475921719873112.

[16]   Z. Tian, S. Howden, Z. Ma, W. Xiao, L. Yu, Pulsed laser-scanning laser Doppler

vibrometer (PL-SLDV) phased arrays for damage detection in aluminum plates,

Mech. Syst. Signal Process. 121 (2019) 158–170.

doi:10.1016/j.ymssp.2018.11.016.

[17]   P. Aryan, A. Kotousov, C.T. Ng, B.S. Cazzolato, A baseline-free and non-contact

method for detection and imaging of structural damage using 3D laser vibrometry,

Struct. Control Heal. Monit. 24 (2017) 1–13. doi:10.1002/stc.1894.

[18]   J.R. Lee, J. Takatsubo, N. Toyama, D.H. Kang, Health monitoring of complex

curved structures using an ultrasonic wavefield propagation imaging system,

Meas. Sci. Technol. 18 (2007) 3816–3824. doi:10.1088/0957-0233/18/12/017.

[19]   M. Ruzzene, S.M. Jeong, T.E. Michaels, J.E. Michaels, B. Mi, Simulation and

measurement of ultrasonic waves in elastic plates using laser vibrometry, in: AIP

Conf. Proc., 2005: pp. 172–179. doi:10.1063/1.1916675.

[20] A. Zak, M. Radzieński, M. Krawczuk, W. Ostachowicz, Damage detection strategies based on propagation of guided elastic waves, Smart Mater. Struct. 21 (2012). doi:10.1088/0964-1726/21/3/035024.

[21] T.J. Saravanan, N. Gopalakrishnan, N.P. Rao, Damage detection in structural element through propagating waves using radially weighted and factored RMS, Measurement. 73 (2015) 520–538. doi:10.1016/j.measurement.2015.06.015.

[22] Y.K. An, H. Sohn, Integrated impedance and guided wave based damage detection, Mech. Syst. Signal Process. 28 (2012) 50–62. doi:10.1016/j.ymssp.2011.11.016.

[23] A.J. Dawson, J.E. Michaels, T.E. Michaels, Isolation of ultrasonic scattering by wavefield baseline subtraction, Mech. Syst. Signal Process. 70–71 (2016) 891–903. doi:10.1016/j.ymssp.2015.09.008.

[24] M. Ruzzene, Frequency-wavenumber domain filtering for improved damage visualization, Smart Mater. Struct. 16 (2007) 2116–2129. doi:10.1088/0964-1726/16/6/014.

[25] T.E. Michaels, J.E. Michaels, M. Ruzzene, Frequency-wavenumber domain analysis of guided wavefields, Ultrasonics. 51 (2011) 452–466. doi:10.1016/j.ultras.2010.11.011.

[26] H. Sohn, D. Dutta, J.Y. Yang, H.J. Park, M. DeSimio, S. Olson, E. Swenson, Delamination detection in composites through guided wave field image processing, Compos. Sci. Technol. 71 (2011) 1250–1256.

doi:10.1016/j.compscitech.2011.04.011.

[27] Y.K. An, B. Park, H. Sohn, Complete noncontact laser ultrasonic imaging for automated crack visualization in a plate, Smart Mater. Struct. 22 (2013) 1–10. doi:10.1088/0964-1726/22/2/025022.

[28] P. Kudela, M. Radzieński, W. Ostachowicz, Identification of cracks in thin-walled structures by means of wavenumber filtering, Mech. Syst. Signal Process. 50–51 (2015) 456–466. doi:10.1016/j.ymssp.2014.05.041.

[29] M.D. Rogge, C.A.C. Leckey, Characterization of impact damage in composite laminates using guided wavefield imaging and local wavenumber domain analysis, Ultrasonics. 53 (2013) 1217–1226. doi:10.1016/j.ultras.2012.12.015.

[30] O. Mesnil, C.A.C. Leckey, M. Ruzzene, Instantaneous and local wavenumber estimations for damage quantification in composites, Struct. Heal. Monit. 14 (2015) 193–204. doi:10.1177/1475921714560073.

[31] A.K. Pandey, M. Biswas, M.M. Samman, Damage detection from changes in curvature mode shapes, J. Sound Vib. 145 (1991) 321–332. doi:10.1016/0022-460X(91)90595-B.

[32] J. Zhou, Z. Li, J. Chen, Damage identification method based on continuous wavelet transform and mode shapes for composite laminates with cutouts, Compos. Struct. 191 (2018) 12–23. doi:10.1016/j.compstruct.2018.02.028.

[33] W. Xu, M. Cao, W. Ostachowicz, M. Radzieński, N. Xia, Two-dimensional curvature mode shape method based on wavelets and Teager energy for damage detection in plates, J. Sound Vib. 347 (2015) 266–278.

doi:10.1016/j.jsv.2015.02.038.

[34]   S. Mohammad, H. Hosseini, C. Willberg, A. Kharaghani, U. Gabbert, Characterization of the guided wave propagation in simplified foam , honeycomb and hollow sphere structures, Compos. Part B Eng. 56 (2014) 553–566. doi:10.1016/j.compositesb.2013.08.077.

[35]   B. Lamboul, D. Osmont, Delamination detection in foam core composite structures using transient flexural wavefields, J. Sound Vib. 366 (2016) 190–198. doi:10.1016/j.jsv.2015.11.042.

[36]   L. Yu, Z. Tian, X. Li, R. Zhu, G. Huang, Core–skin debonding detection in honeycomb sandwich structures through guided wave wavefield analysis, J. Intell. Mater. Syst. Struct. 30 (2019) 1306–1317. doi:10.1177/1045389X18758180.

[37]   Z. Su, L. Ye, Lamb wave propagation-based damage identification for quasi-isotropic CF/EP composite laminates using artificial neural algorithm: Part II-implementation and validation, J. Intell. Mater. Syst. Struct. 16 (2005) 113–125. doi:10.1177/1045389X05047600.

[38]   F. Li, G. Meng, K. Kageyama, Z. Su, L. Ye, Optimal mother wavelet selection for Lamb wave analyses, J. Intell. Mater. Syst. Struct. 20 (2009) 1147–1161. doi:10.1177/1045389X09102562.